Topology Optimization of Stressed Capacitive RF MEMS Switches

Mandy A. Philippine, Ole Sigmund, Gabriel M. Rebeiz, *Fellow, IEEE*, and Thomas W. Kenny

***Abstract*—Geometry design can improve a capacitive radio-frequency microelectromechanical system switch's reliability by reducing the impacts of intrinsic biaxial stresses and stress gradients on the switch's membrane. Intrinsic biaxial stresses cause stress stiffening, whereas stress gradients cause out-of-plane curling. We use topology optimization to systematically generate designs, by minimizing stress stiffening, minimizing curling, or minimizing stress stiffening while constraining the curling behavior. We present the corresponding problem formulations and sensitivity derivations and discuss the role of key elements in the problem formulation. [2012-0130]**

***Index Terms*—Geometry design, intrinsic stress, mechanical design, radio-frequency microelectromechanical systems (RF MEMS), stress gradient, topology optimization.**

I. Introduction

THE MECHANICS of microelectromechanical systems (MEMS) are typically designed using a set of popular building blocks (rectangular cantilevers, folded flexure beams, crab legs, etc.). Optimization of these structures or their variants is often performed using scaling laws, parametric optimization, or some insight gained from studying relationships between certain features and a device's behavior. Topology optimization is a more powerful tool that systematically generates the full topology of a design, including the size, shape, and location of features, and can satisfy several goals despite potentially complex relationships. This paper demonstrates the method for an RF switch and provides the appropriate problem formulation to reduce stress sensitivity of a membrane with multiple anchors.

The radio-frequency MEMS (RF MEMS) community has been working on designs of stress-insensitive capacitive RF switches. Like many other MEMS devices, their switches experience both curling from stress gradients across the thickness of the membrane and stress stiffening from in-plane biaxial stresses. The stresses are typically a result of the fabrication process and can vary from wafer to wafer or within a single wafer. In the case of RF switches, reliability is compromised by stress variations: The actuation voltage is sensitive to both in-plane stresses that cause stress stiffening and to stress gradients that affect the air gap.

A range of successful solutions have been provided to compensate for stress and the related temperature sensitivity problems. Mahameed and Rebeiz proposed a switch that translates in-plane stress variations to in-plane motion rather than vertical deflections by increasing thickness, maintaining structural beam widths to a minimum and introducing asymmetry to encourage motion in a specific direction [1]. Meander spring designs have been suggested [2]. Goldsmith *et al.* used a molybdenum membrane, bringing the membrane's thermal expansion constant closer to the substrate's [3]. Electrical compensation was demonstrated in [4]. Using parametric optimization, Reines *et al.* [5] systematically demonstrated the tradeoff between stress stiffening and vertical deflections for a symmetric circular switch with cutouts and vertical springs. Nieminem *et al.* used cutouts as well, but also justified anchor placement with results from finite-element analysis [6]. Mahameed and Rebeiz [7] demonstrated a highly stress- and temperature-insensitive switch with elements from [5] and [6]. This paper extends their work: Topology optimization is used to systematically generate the size, shape, and location of cutouts and of the overall structure. Finite-element analysis and its derived results are iteratively used with an optimizer to design novel switch geometries.

Section II presents topology optimization and its implementation. Section III describes the finite-element model. Section IV provides the problem formulations and sensitivity equations. An example problem is defined in Section V, and a set of solutions is presented and compared with an existing design in Section VI. An intuitive interpretation of the resulting topologies is provided, as well as a discussion on the quality of the designs obtained via topology optimization.

II. Topology Optimization

A. Background

Topology optimization can help design the topology of a mechanical device. In its most popular form, the technique minimizes the mechanical compliance of a structure by varying the distribution of material within a design space [8]. Private companies such as Airbus and Boeing have adopted

Manuscript received May 18, 2012; revised September 1, 2012; accepted October 7, 2012. Date of publication November 16, 2012; date of current version January 30, 2013. This work was supported in part by the National Science Foundation Graduate Research Fellowship Program and in part by the Defense Advanced Research Projects Agency Nanoelectromechanical/Microelectromechanical S&T Fundamentals program under Grant N66001-10-1-4006, issued by the Space and Naval Warfare Systems Center Pacific (SPAWAR). Subject Editor C. T.-C. Nguyen.

M. A. Philippine and T. W. Kenny are with the Mechanical Engineering Department, Stanford University, Stanford, CA 94305 USA (e-mail: mandyp@stanford.edu; tkenny@stanford.edu).

O. Sigmund is with the Mechanical Engineering Department, Technical University of Denmark (DTU), 2800 Lyngby, Denmark (e-mail: sigmund@mek.dtu.dk).

G. M. Rebeiz is with the Electrical Engineering Department, University of California, San Diego, CA 92093 USA (e-mail: rebeiz@ece.ucsd.edu).

Digital Object Identifier 10.1109/JMEMS.2012.2224640

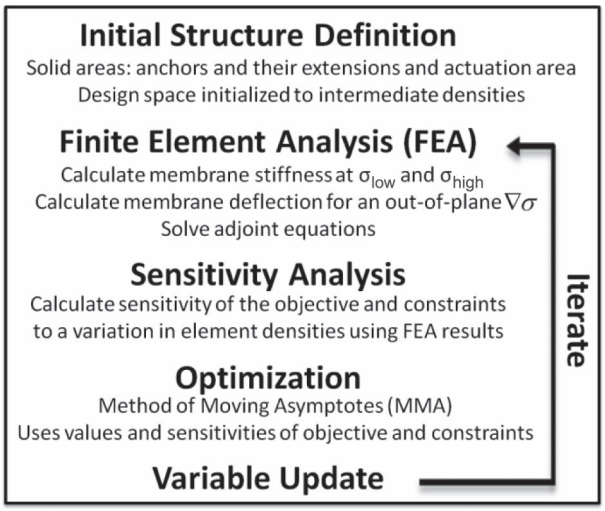

Fig. 1. Basic topology optimization process flow.

the method to optimize products [9], [10] using commercial software dedicated to topology optimization such as Altair or FE-Design. Beyond the traditional minimum compliance problem, this technique has been employed in academic settings to solve a broad range of problems [8], including some in the MEMS domain [11]–[14]. The basic process and tools remain similar from application to application, but the specific problem formulations vary. Defining a new problem formulation usually also involves finding practical sensitivity expressions.

B. Method Overview

The basic topology optimization process flow is shown in Fig. 1. First, the design area is defined and discretized. The material properties, support conditions, intrinsic stresses, and stress gradients are also predefined.

The solid isotropic material with penalization model (SIMP) is used such that the design variables are the individual physical element densities $\overline{\widetilde{\rho}}_e$: A null density represents an absence of material, whereas a density of value 1 represents the presence of material. Penalized intermediate density values are permitted such that the optimization variables are continuous. Element-level material properties and internal stress values are weighed by the individual densities, raised to the power of p, which is the penalization factor. p is typically set to 3 and depends on Poisson's ratio [8].

Once the design space has been properly set up, finite-element analysis is performed for an initial guess. The design space densities are typically initialized to some intermediate density. Next, the sensitivity of the objective function and of the constraints to variations in the element densities are calculated using the resulting solution and any associated adjoint solutions.

The mathematical programming method, i.e., method of moving asymptotes (MMA), uses the objective and constraint values and sensitivities to provide an updated density distribution [15].

Finite-element analysis followed by sensitivity analysis and optimization with MMA are performed for this new structure to obtain a new updated density distribution. This process is repeated until the difference between consecutive density distributions is small [8].

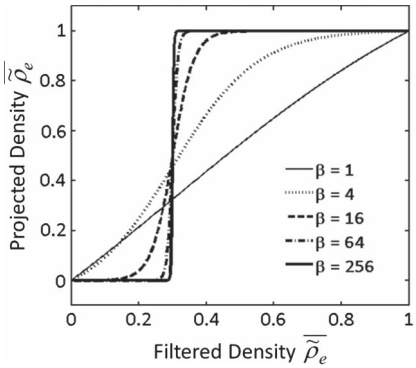

Fig. 2. Filtering scheme. Plot of (3) for a threshold parameter $\boldsymbol{\eta = 0.3}$ and various projection parameters $\boldsymbol{\beta}$.

C. Filtering and Projection

Filtering is implemented to prevent well-known numerical problems such as checkerboarding and mesh dependence. The filtering scheme from [16] is used here. The filtered variables $\widetilde{\rho}_e$ are weighted averages of neighboring variables ρ_e, i.e.,

$$\widetilde{\rho}_e = \frac{\Sigma_{j\in\mathbb{N}_{s,e}} w(x_j) v_j \rho_j}{\Sigma_{j\in\mathbb{N}_{s,e}} w(x_j) v_j} \tag{1}$$

where $\mathbb{N}_{s,e}$ is the set of neighboring elements, defined as the set of elements lying within a circle of radius $r_{\min}$ centered on the element e. $w(x_j)$ is the weighting function, i.e.,

$$w(x_j) = r_{\min} - |x_j - x_e| \tag{2}$$

where $\boldsymbol{x_j}$ and $\boldsymbol{x_e}$ are the coordinates of the center of elements $\boldsymbol{j}$ and $\boldsymbol{e}$, respectively.

A threshold projection ensures convergence toward a solid/void solution. The projected densities $\overline{\widetilde{\rho}}_e$, which are termed "physical densities," are [16]

$$\overline{\widetilde{\rho}}_e = \frac{\tanh(\beta\eta) + \tanh\left(\beta(\widetilde{\rho}_e - \eta)\right)}{\tanh(\beta\eta) + \tanh\left(\beta(1-\eta)\right)} \tag{3}$$

where β is the projection parameter, and η is the threshold value. We increase β periodically such that the design gradually converges toward a solid/void solution. Fig. 2 plots the projection scheme for several values of β with an example threshold value $\eta = 0.3$.

The sensitivity expressions incorporate the filter and projection and are obtained using the chain rule

$$\frac{\partial f}{\partial \rho_j} = \Sigma_{e\in\mathbb{N}_{s,j}} \frac{\partial f}{\partial \overline{\widetilde{\rho}}_e} \frac{\partial \overline{\widetilde{\rho}}_e}{\partial \widetilde{\rho}_e} \frac{\partial \widetilde{\rho}_e}{\partial \rho_j}. \tag{4}$$

D. Robust Optimization

Robust optimization helps enforce a minimum feature size for both solid and void areas [16]. The minimum feature size is set by the fabrication process and is controlled in the

optimization by $r_{\min}$. A robust problem considers three designs simultaneously: a dilated design, an intermediate design, and an eroded design, obtained from using projection parameter values of $\eta = \eta^* < 0.5$, $\eta = 0.5$, and $\eta = 1 - \eta^*$, respectively. The final solution is the converged intermediate design. A previous paper demonstrates the importance of robust optimization for convergence toward a design that can be fabricated [17].

E. Basic Model

The entire optimization problem is solved within MATLAB, including the finite-element analysis. The code is based on pieces of code from DTU [18], by Bhatti [19], and by Svanberg [15], which provided the basic topology optimization structure, the basic finite-element simulation, and the MMA optimizer, respectively. The finite-element code was enhanced to support variable density distributions and the stress stiffening and curling behaviors. The DTU code was enhanced to include filtering, projection, and robust optimization. The overall code was adapted to solve the three problems discussed in Section IV.

Once optimized designs are obtained, they are postprocessed: CAD-compatible files are created from the converged density distributions using the img2cad software. The boundaries between solid and void areas are then smoothed, and the quality of the solutions is verified with the commercial finite-element program COMSOL.

III. Finite-Element Model

A. Stress Stiffening

A structure's stiffness changes as a function of its membrane stresses. Thin films grown in a MEMS fabrication process typically develop in-plane biaxial stresses, which can result in stress stiffening. These can vary across a wafer and from wafer to wafer but are assumed to be uniform within each device.

Cook *et al.* outlined a method to model this behavior using the finite-element method [20]. A stress stiffness matrix K_σ and a stress force vector F_σ are added to the original stiffness matrix K and to the external force vector F, respectively, such that

$$(K + K_\sigma)u = F + F_\sigma. \tag{5}$$

The stress force vector is assembled from the element-level expression

$$\{f_\sigma\}_e = -\int B_e^T \{\sigma_0\}_e dv \tag{6}$$

where B_e is the usual strain-displacement matrix. The stress stiffness matrix is assembled from the element-level expression

$$\{k_\sigma\}_e = \int G_e^T S_e G_e dv \tag{7}$$

where G contains derivatives of the shape functions, and S contains the stress levels of elements in response to the stress force vector only. These stresses are strongly dependent on boundary conditions and are found by solving

$$Ku_\sigma = F_\sigma. \tag{8}$$

During assembly of F_σ and K_σ, the element-level vectors and matrices are weighed by their corresponding physical densities $\widetilde{\overline{\rho}_e}$, raised to the power p.

B. Curling

Curling occurs in membranes with stress gradients, which can arise within a thin film as a result of the fabrication process, or in laminated plates with asymmetric stresses in the layers. In both cases, the behavior is modeled by adding internal moments m_x and m_y to the force vector. On an element level, these moments are given by [20]

$$m_x = \int_{-t/2}^{t/2} \sigma_x z \, dz \qquad m_y = \int_{-t/2}^{t/2} \sigma_y z \, dz \tag{9}$$

where the stresses σ_x and σ_y are functions of the normal dimension z and are determined by the stress gradient $\nabla\sigma$. The thickness of the membrane is denoted by t. These moments are weighed by the physical element densities $\widetilde{\overline{\rho}_e}$ and assembled into the force vector $F_{\nabla\sigma}$. The curling displacements are found by solving

$$Ku_{\nabla\sigma} = F_{\nabla\sigma}. \tag{10}$$

Note that curling could be observed in membranes free of stress gradients that experience in-plane biaxial stresses. These deflections could be due to buckling, nonrigid anchors, or initially deflected membranes. We assume ideal boundary conditions, a flat membrane, and no buckling for the purpose of this optimization and, therefore, only consider curling behavior due to stress gradients.

IV. Problem Formulations and Sensitivity Expressions

Four formulations are presented. The first minimizes the compliance of a prestressed plate and is the formulation provided in [21]. The second minimizes curling, without taking stress stiffening into account, and is a simplified version of the formulation published in [22]. The third minimizes the stress stiffening behavior, without considering the curling behavior and was presented in [17]. The fourth combines the two previous formulations to minimize stress stiffening while constraining curling.

A. Minimizing Compliance

Minimizing compliance of a prestressed plate consists in minimizing the work done by external forces. The objective is expressed as [21]

$$f_0 = \frac{1}{2} F^T (u - u_\sigma). \tag{11}$$

A volume constraint is imposed, i.e.,

$$f_1 = \frac{\Sigma \widetilde{\overline{\rho}_e} v_e}{\Sigma \, v_e} - v^* < 0 \tag{12}$$

where v^* is a given volume fraction, v_e is the volume of an element e, and the sums are conducted over all elements in the design area. In a robust optimization, one would use a min–max formulation

$$\text{Minimize}: \ \max\{\{f_0\}_{\text{eroded}}, \{f_0\}_{\text{interm}}, \{f_0\}_{\text{dilated}}\} \quad (13)$$

and apply the volume constraint to the dilated solution.

The sensitivity analysis for this objective and constraint can be found in [8], [21] and yields the following expressions:

$$\frac{df_0}{d\widetilde{\widetilde{\rho}}_e} = \lambda_1^T\left(\frac{dF_\sigma}{d\widetilde{\widetilde{\rho}}_e} - \frac{dK}{d\widetilde{\widetilde{\rho}}_e}u - \frac{\partial K_\sigma}{\partial\widetilde{\widetilde{\rho}}_e}u\right) + \lambda_2^T\left(\frac{dF_\sigma}{d\widetilde{\widetilde{\rho}}_e} - \frac{dK}{d\widetilde{\widetilde{\rho}}_e}u_\sigma\right) \quad (14)$$

$$\frac{df_1}{d\widetilde{\widetilde{\rho}}_e} = \frac{v_e}{\Sigma v_e} \quad (15)$$

where the multipliers λ_1 and λ_2 are chosen such that

$$(K + K_\sigma)\lambda_1 = \frac{1}{2}F \quad (16)$$

$$K\lambda_2 = -\frac{1}{2}F - \frac{\partial(\lambda_1^T K_\sigma)}{\partial u_\sigma}u. \quad (17)$$

B. Minimizing Curling

To minimize curling, the objective function is set to the weighted power of the deflection given by [22]

$$f_2 = (u_{\nabla\sigma}^T)A(u_{\nabla\sigma}) \quad (18)$$

where $u_{\nabla\sigma}$ is found from (10), and A is a diagonal matrix for which each diagonal term that is associated with a normal displacement degree of freedom is a nodal density raised to the third power. A nodal density is an average of the surrounding element densities. It is raised to the third power to penalize intermediate densities.

The volume constraint f_1 is imposed in this formulation as well. Robust optimization is implemented as in the previous formulation, with a min–max formulation and enforcement of the volume constraint for the dilated design.

The sensitivity analysis for this objective can be found in [22]. Note, however, that it is assumed here that the displacements caused by the stress gradient are not sufficient to induce stress stiffening. The sensitivity of the objective is therefore simplified to

$$\frac{df_2}{d\widetilde{\widetilde{\rho}}_e} = \left\{u_{\nabla\sigma}^T\right\}\frac{dA}{d\widetilde{\widetilde{\rho}}_e}\{u_{\nabla\sigma}\} + \left\{\lambda_3^T\right\}_e\left(\frac{d[F_{\nabla\sigma}]_e}{d\widetilde{\widetilde{\rho}}_e} - \frac{d[K]_e}{d\widetilde{\widetilde{\rho}}_e}\{u_{\nabla\sigma}\}_e\right). \quad (19)$$

The adjoint equation is

$$K\lambda_3 = 2A\,u_{\nabla\sigma}. \quad (20)$$

C. Minimizing Stress Stiffening

For the structures and stress levels considered, in-plane displacements caused by the intrinsic biaxial stresses are small compared with the in-plane dimensions. Thus, for a given set of boundary conditions and given stress states σ_{high} and σ_{low}, the stiffness shift $k_{\text{high}} - k_{\text{low}}$ is proportional to the stress change. It is therefore sufficient to consider only two stress states, and the objective is chosen to be the percent change in stiffness between them, i.e.,

$$\frac{(k_{\text{high}} - k_{\text{low}})}{k_{\text{low}}} = \frac{k_{\text{high}}}{k_{\text{low}}} - 1. \quad (21)$$

This is equivalent to minimizing the stiffness ratio $k_{\text{high}}/k_{\text{low}}$ since k_{high} will always be greater than k_{low}. It follows from the formulation of the minimum compliance of a prestressed plate and from the fact that stiffness is simply the inverse of compliance that minimizing this stiffness ratio can be achieved by minimizing the following function:

$$f_3 = \frac{F^T(u - u_\sigma)_{\text{low}}}{F^T(u - u_\sigma)_{\text{high}}} \quad (22)$$

where u and u_σ are independently calculated for both the low and high stress states. Once again, a min–max formulation is used.

This optimization problem needs a constraint to eliminate the trivial solution, which would completely isolate the forced area from the anchors, resulting in null stiffness at all stress states. The solution would be a floating membrane that does not make physical sense. Therefore, an upper bound S^* is enforced on the structure's compliance. The compliance constraint is applied to the eroded solution at the lower stress state, i.e.,

$$f_4 = \{F^T u_{\text{low}}\}_{\text{eroded}} - S^* < 0. \quad (23)$$

The volume constraint is applied to the dilated solution. The procedure outlined in [21] can be used to find the sensitivity of the objective function to variations of the physical density $\widetilde{\widetilde{\rho}}_e$ of each element, i.e.,

$$\begin{aligned}\frac{df_3}{d\widetilde{\widetilde{\rho}}_e} = {} & \left(\left\{\lambda_4^T\right\}_e + \left\{\lambda_6^T\right\}_e\right)\frac{d[F_{\sigma,\text{low}}]_e}{d\widetilde{\widetilde{\rho}}_e} \\ & + \left(\left\{\lambda_5^T\right\}_e + \left\{\lambda_7^T\right\}_e\right)\frac{d[F_{\sigma,h}]_e}{d\widetilde{\widetilde{\rho}}_e} \\ & - \left\{\lambda_4^T\right\}_e\frac{d[K]_e}{d\widetilde{\widetilde{\rho}}_e}\{u_{\text{low}}\}_e - \left\{\lambda_5^T\right\}_e\frac{d[K]_e}{d\widetilde{\widetilde{\rho}}_e}\{u_h\}_e \\ & - \left\{\lambda_6^T\right\}_e\frac{d[K]_e}{d\widetilde{\widetilde{\rho}}_e}\{u_{\sigma,\text{low}}\}_e - \left\{\lambda_7^T\right\}_e\frac{d[K]_e}{d\widetilde{\widetilde{\rho}}_e}\{u_{\sigma,h}\}_e \\ & - \frac{\partial\left(\left\{\lambda_4^T\right\}_e\right)}{\partial\widetilde{\widetilde{\rho}}_e}\{u_{\text{low}}\}_e - \frac{\partial\left(\left\{\lambda_5^T\right\}_e\right)}{\partial\widetilde{\widetilde{\rho}}_e}\{u_h\}_e. \end{aligned} \quad (24)$$

The adjoint equations used to obtain λ_4, λ_5, λ_6, and λ_7 are

$$(K + K_{\sigma,\text{low}})\lambda_4 = \frac{1}{F^T u_h}F \quad (25)$$

$$(K + K_{\sigma,h})\lambda_5 = -\frac{F^T u_{\text{low}}}{(F^T u_h)^2}F \quad (26)$$

$$K\lambda_6 = \frac{\partial(\lambda_4^T K_{\sigma,\text{low}})}{\partial u_{\sigma,\text{low}}}u_{\text{low}} - \frac{1}{F^T u_h}F \quad (27)$$

$$K\lambda_7 = -\frac{\partial(\lambda_5^T K_{\sigma,h})}{\partial u_{\sigma,h}}u_h + \frac{F^T u_{\text{low}}}{(F^T u_h)^2}F. \quad (28)$$

D. Minimizing Stress Stiffening With a Constraint on Curling

The previous formulations are building blocks for the one that can be used to design stress-insensitive capacitive RF

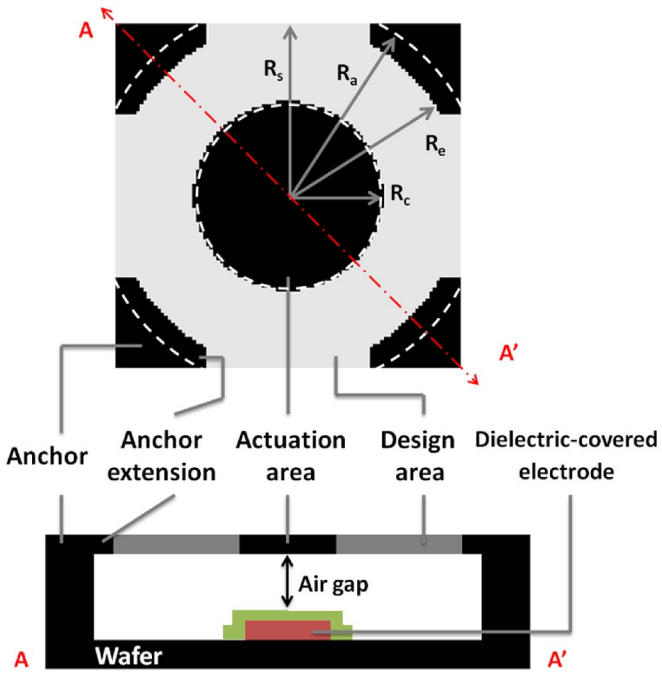

Fig. 3. Top and cross-sectional views of circular RF MEMS switch with definition of design space areas and dimensions. $R_c = 50$ μm, $R_e = 91$ μm, $R_a = 100$ μm, and $R_s = 92$ μm. White dotted lines delineate the actuation area and the anchors.

switches. In this formulation, the goal is to minimize the stress stiffening behavior while constraining the curling. A min–max formulation is employed once again, with the objective set to f_3. A compliance constraint f_4 is applied to the eroded solution at the low stress state. A curling constraint is also applied to the eroded, intermediate, and dilated density distributions such that

$$f_5 = f_2 - P^* < 0 \tag{29}$$

where P^* is a given weighted power of deflection. A volume constraint is unnecessary and, therefore, not included.

V. Example Problem

A. Definition of Design Space

The design setup considered for optimization is shown in Fig. 3. Anchors are locations where the membrane is fixed to the wafer. Anchor extensions are parts of the membrane surrounding the anchors that need to be solid for fabrication purposes. The actuation area is an area of the membrane that is electrostatically actuated when a bias is applied to the electrode directly beneath it. The anchors, anchor extensions, and actuation area are set to have density 1 and cannot be modified. All other areas comprise the design space and will be optimized.

Four anchors are positioned 100 μm from the center and span 44° each. The circular central actuation area has a 50-μm radius. The anchor extensions and their dimensions are shown in Fig. 3. The thickness t is set to 0.5 μm. The membrane is gold: The elastic modulus E is set to 45 Gpa, and the Poisson ratio is set to 0.45. This setup is chosen such that it matches the one from a switch designed by Reines *et al.* for low stress sensitivity [5]. This permits comparison of topology optimized designs to an existing switch geometry. His switch has a step in the membrane due to the fabrication process. This step was not modeled for the topology optimized designs. All comparisons are therefore made to a flat version of Reines' switch, which has been simulated in COMSOL. The step in his design reduces sensitivity to stress gradients. To extend this work, a 3-D topology optimization could choose the placement of such steps to further minimize curling.

B. Finite-Element Setup

A quarter of the structure is modeled and optimized, and symmetry conditions are applied. Clamped boundary conditions are enforced at the anchors. Each setup is discretized using a square mesh with 50 elements to a side.

Rectangular Mindlin plate elements with three translation and three rotation degrees of freedom per node are used. These elements are more appropriate than 3-D solid elements since the capacitive RF switches are flat membranes actuated out of plane and the thickness is several orders of magnitude smaller than the in-plane dimensions. The 2-D solid elements are capable of capturing displacements in the normal direction. Although the Kirchhoff plate theory is more accurate for thin plates, Mindlin elements are employed here for their ease of implementation and relatively low computational cost. In addition, they have been successfully used in the past for similar applications [22]. The membrane and bending parts of the stiffness matrices are calculated with four Gauss points, whereas the shear part is calculated with just one to prevent shear locking.

Stress stiffening and curling are independently modeled, as outlined in Section III-A and B. Stress stiffening is analyzed for the two stress levels $\sigma_{\text{low}} = 100$ MPa and $\sigma_{\text{high}} = 180$ MPa, such that the various objectives and constraints discussed in Section IV may be calculated. A uniform mechanical pressure is applied in the actuation area to model electrostatic forcing. The stiffness is obtained by applying a small force on the actuation area such that the membrane does not experience geometric nonlinearities from large displacements. This simplification is justified by a finding by Buhl *et al.* [23]: They obtained only marginally better results when they incorporated geometric nonlinearities into their topology optimization as compared with those obtained with linear analysis. Although more computationally demanding, the nonlinear analysis is feasible and could be incorporated into future work. Curling is modeled for a stress gradient set to $\nabla\sigma = 12$ MPa/μm applied to the entire membrane.

C. Optimization Parameters

The same 2500 elements used for finite-element modeling are also assigned a density variable ρ_e. The radius of neighboring elements $r_{\min}$, which is used for the density filter, is set to 5. The projection parameter β is initially set to 1 and incremented by a factor of 1.5 either every 50 iterations or when the change between two consecutive iterations falls below one percent. If the constraints are not met after 50 iterations, β is reduced by a factor of 0.7. We stop incrementing β after it becomes greater than 500. The threshold parameter η is set to 0.3 for the dilated design, 0.5 for the intermediate design, and 0.7 for the eroded

TABLE I
OPTIMIZATION PARAMETERS AND RESULTS

		Optimization Parameters			Converged solution characteristics, in Matlab					
Label	Design process	v^*	$S^*/S_{\min}$	$P^*/P_{\min}$	f_0	f_1	f_2	f_3	f_4	f_5
a	none									
b	Intuition									
c	Formulation A	0.8			0.0074	-6×10^{-5}				
d	Formulation B	0.55				-0.03	16.6			
e	Formulation C	0.5	2.7			-0.05		1.71	-4×10^{-4}	
f	Formulation C	0.5	67.6			-0.1		1.66	-0.1	
g	Formulation C	0.8	40.5			-0.1		1.68	-0.09	
h	Formulation C	0.8	2.7			-0.04		1.68	-3×10^{-4}	
i	Formulation D		27	3.6				1.70	-0.1	-3
j	Formulation D		27	6				1.60	-0.1	-4
k	Formulation D		27	12				1.64	-0.05	-10
m	Formulation D		27	30				1.68	-0.04	-217

design. The dilated volume fraction constraint v^* is set to either 0.5 or 0.8 for the problem described in Section IV-B where curling behavior is minimized. The compliance constraint S^* is chosen based on $S_{\min}$, i.e., the strain energy of the minimum compliance design with a prestress of σ_{low}. The flatness constraint P^* is chosen based on $P_{\min}$, i.e., the weighted power of deflection of the design obtain from minimizing curling. The parameter values used for the optimizations presented here are summarized in Table I.

D. Demonstration of the Topology Optimization Process

Plots of the intermediate density distribution of the circular switch at several stages of an optimization are shown in Fig. 4. Formulation D was used in this example, with the constraint on the compliance of the eroded density distribution set to $S^*/S_{\min} = 27$ and the constraint on the power of deflection of the eroded, intermediate, and dilated distributions all set to $P^*/P_{\min} = 12$.

Black areas are solid, whereas white areas are void. Gray areas have elements with intermediate densities. In the initial density distribution, the anchors, anchor extensions, and actuation area are solid. They remain solid during the entire optimization process.

Initially, the design space is entirely gray because the initial guess has densities initialized to 0.1 in that area. In the first phase of the optimization, intermediate densities are penalized very little through the penalization factor but not through the filtering scheme. There is no solid connection between the anchors and actuation area when β is low because the intermediate density elements provide sufficient stiffness to satisfy the constraints. After the 5th iteration, areas adjacent to the actuation area start to have lower density values. By the 100th iteration, there is a donut-shaped region of low-density elements surrounding the actuation area.

As the projection parameter β increases, intermediate density values are projected to either null or full density. The low-density donut is no longer stiff enough to satisfy the compliance constraint. By the 200th iteration, high-density bridges have formed between the solid area already connected to the anchors and the actuation area. By the 400th iteration, the bridges are fully solid, and the hole shapes have evolved in an attempt by the optimizer to decrease the objective function.

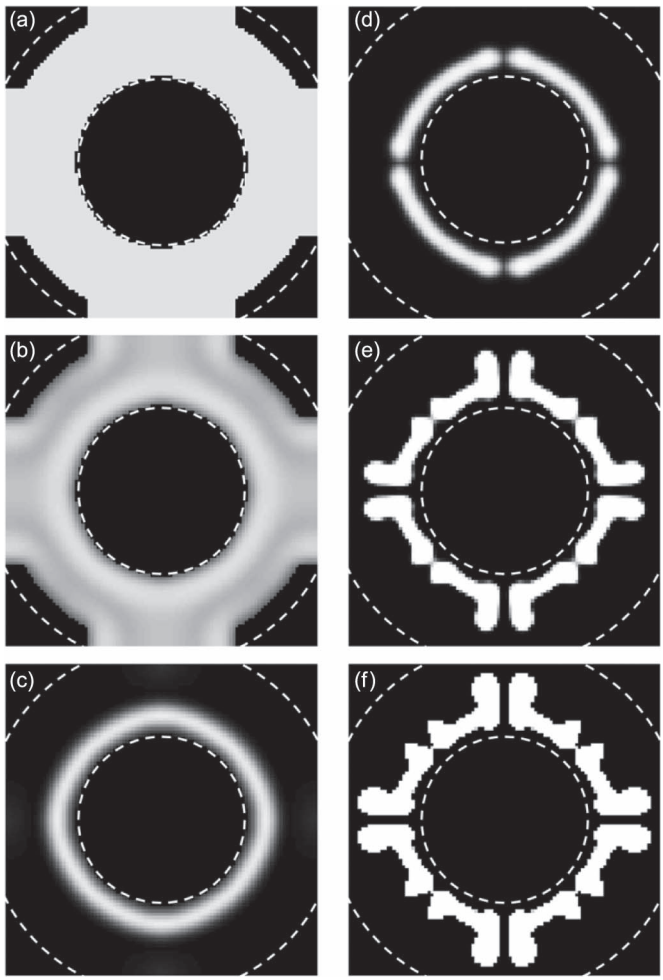

Fig. 4. Plots of density distributions at several iterations. White dotted lines delineate the actuation area and the anchors. (a) Initial guess. (b) Iteration 5. (c) Iteration 100. (d) Iteration 200. (e) Iteration 400. (f) Final converged solution, iteration 693.

In the converged solution, β is large enough that a nearly solid/void solution is obtained. Between the 400th iteration and the final 693rd iteration, boundaries become better defined. In this particular example, four small connections with intermediate densities exist in addition to the four main connections in the 400th iteration. They have disappeared in the converged density distribution.

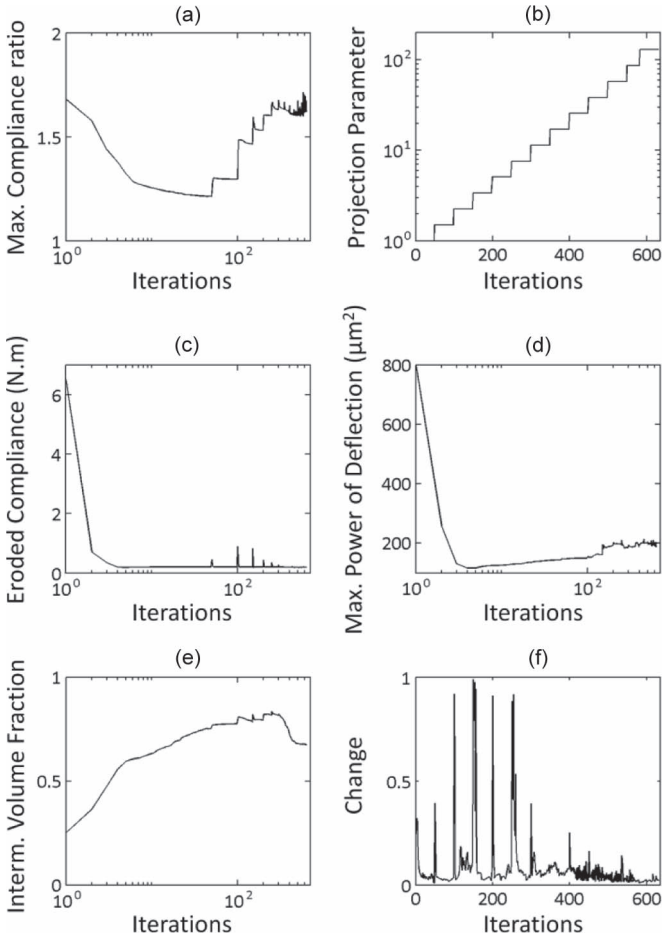

Fig. 5. Plots of key parameters at each iteration.

The evolution of the objective function, of constraint values, and of other key parameters during the optimization is plotted in Fig. 5. Log scales are used in some plots for clarity. The objective function, the ratio of compliance at σ_{high} to σ_{low}, is plotted in Fig. 5(a) for the intermediate density distribution. It decreases as expected when the constraints are satisfied and for a given β. The evolution of the projection parameter β is shown in Fig. 5(b). Fig. 5(c) plots the compliance of the eroded density distribution. Fig. 5(d) plots the maximum of the powers of deflection of the dilated, intermediate, and eroded density distributions. These plots show that the constraints are initially satisfied within five iterations. Every time β is increased, the objective function may experience a jump since solutions with intermediate densities are favored by this objective. In addition, the β increase may result in violation of the constraints, which is corrected within a few iterations. This explains the spikes in the objective, constraints, and in the amount of change, after some increases in β. The amount of change between consecutive unfiltered density distributions is shown in Fig. 5(f). The volume fraction is not constrained in this formulation. However, it takes on reasonable values, as shown in Fig. 5(e), and never approaching 0 or 1. This indicates that the problem is well defined despite the absence of a volume constraint. The algorithm, therefore, works as expected.

In general, the algorithm is better behaved for lower values of β. When β is large, significant material redistribution cannot occur, effectively reducing the optimizer's ability to reduce the objective function and satisfy the constraints. Oscillations can occur and are observed here as the minor connections previously mentioned are alternately made solid or void, until a void area is chosen in the converged solution. These oscillations could be minimized by increasing β more slowly.

Guest *et al.* proposed two methods to eliminate the need for a continuation method on β [24]. First, he suggests fixing β to a constant large value and tightening the initial MMA asymptotes. This results in more conservative MMA approximations and in smaller initial design steps. The solution becomes highly dependent on the initial guess, which reduces the design space, often leading the solution toward low-quality local minima. In addition, a large β increases the risk of numerical instabilities caused by regions containing intermediate densities, which are common in the initial iterations when the algorithm is searching for a compromise between the objective and the curling constraint. Second, he proposes increasing the upper bound $\rho_{\max}$ on the variables ρ_e to approach the Heaviside function with ρ_e rather than with β, which can then remain small. The Heaviside function given in [24] is not compatible with robust optimization because it is specific to a threshold value of $\eta = 0$. We generalize the method to project densities $\widetilde{\rho_e}$ using

$$\overline{\widetilde{\rho}_e} = \frac{\tanh(\beta\eta) + \tanh\left(\beta(\widetilde{\rho}_e/\rho_{\max} - \eta)\right)}{\tanh(\beta\eta) + \tanh\left(\beta(1-\eta)\right)} \tag{30}$$

instead of (3). The algorithm did not converge after 1000 iterations with the constraints set to $S^*/S_{\min} = 27$ and $P^*/P_{\min} = 6$. In addition, obtaining high-quality solutions would require tuning for optimal β and $\rho_{\max}$, further increasing the computational cost. For the formulation proposed in Section IV-D, we therefore keep a continuation method on β.

VI. Results and Discussion

A. Presentation of Results

Twelve designs are shown in Fig. 6. The out-of-plane deflections caused by a 12 MPa/μm stress gradient in the z-direction are plotted on each design, as simulated in the finite-element software COMSOL. Design a has a fully solid design space and is included to compare its performance with that of switches with cutouts. Design b is a planar version of the switch in [5] and is included since it has been published as a stress-insensitive switch and its boundary conditions and actuation areas were used to obtain the topology optimized designs. All other designs were obtained using topology optimization followed by minor postprocessing. The postprocessing step smoothens the lines and removes unnecessary material that may be left over from modifications made during the high β phase without affecting design performance. Design c is the result of the minimum compliance of a prestressed plate given by formulation A and at the stress level σ_{low}. The minimum curling formulation B yielded design d with a volume constraint set at $v^* = 0.5$. Designs e–h were obtained using the minimum stiffening formulation C. Designs i–m were generated using the minimum stiffening formulation D with a curling constraint, with various values of P^*. The constraint values are included

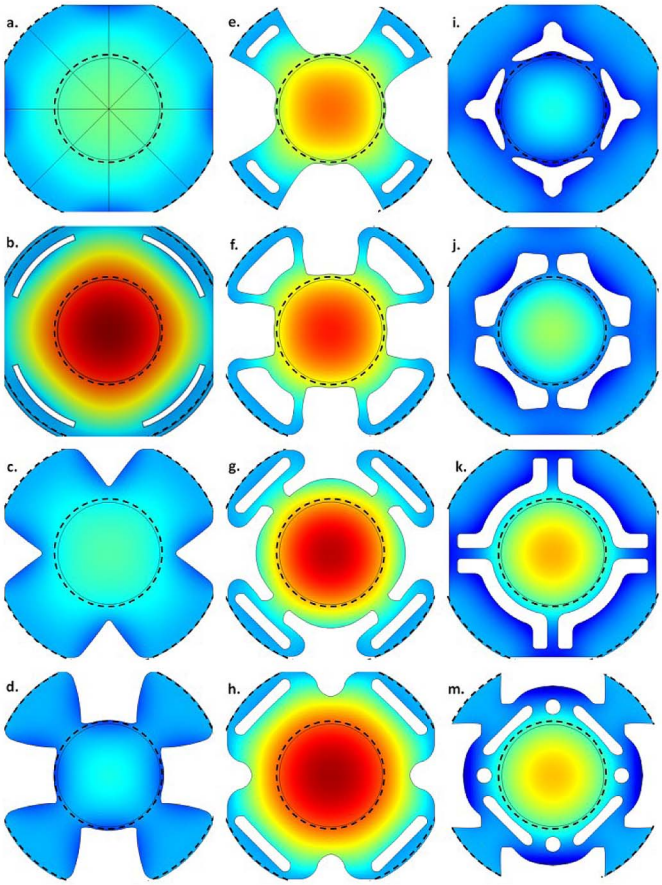

Fig. 6. Plots of the simulated deflections of circular capacitive RF switches subjected to a 12-MPa/μm stress gradient across their thickness (z-direction). The anchors are clamped. Displacements range from dark red at -350 nm to dark blue at $+150$ nm. Black dotted lines delineate the actuation area and the anchors.

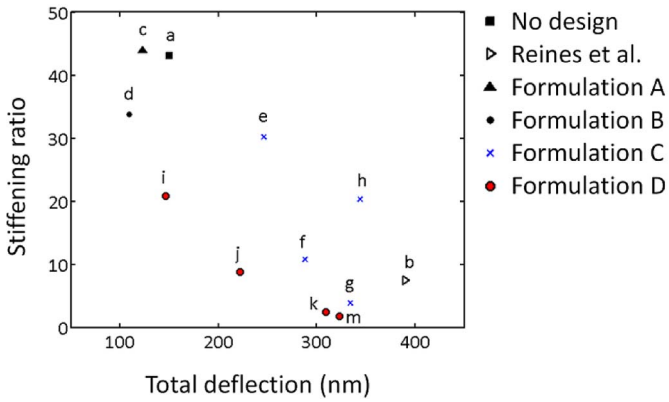

Fig. 7. Plot of the stress stiffening and curling behaviors.

in Table I. The function values f_0 through f_5 of the converged density distribution are also included in Table I. These functions are defined in Section IV and are calculated within MATLAB. f_0 found for design c becomes $C_{\min}$, and f_2 found for design d becomes $P_{\min}$. f_1, f_4, and f_5 are constraints and should be negative to be satisfied. f_3 is the objective function used for formulations C and D.

The design performances are compared with each other in Fig. 7 in terms of their stress stiffening and curling behaviors. Whereas for the purpose of optimization, the stress stiffening and curling behaviors were characterized in terms of compliance and powers of deflection, defined by (11) and (18); they are characterized in Fig. 7 with the more commonly encountered quantities. The stress stiffening behavior is characterized by the ratio of the stiffness k_2 caused by a residual stress value of 100 MPa to the stiffness k_1 of the structure not subjected to any stress. The total stiffness is $k_1 + k_2$ [25]. Stiffness is defined here for a small force as the quotient of the total force applied out of plane to the actuation area and the resulting normal displacement at the center of the membrane. The curling behavior is characterized in Fig. 7 by the total vertical difference between the highest and lowest points of the deformed structure when it is subjected to a 12-MPa/μm stress gradient in the z-direction. No in-plane biaxial stresses are included in the curling analysis.

B. Optimized Topologies

The minimum compliance structure is more or less an assembly of four wide beams running from the anchors to the actuation area. It resembles other published results [21], although direct comparison is not possible given differing boundary conditions. This optimization provides a reference value $S_{\min}$ with which the compliance constraints in the other formulations are compared.

The minimum curling structure is the flattest one in the set. The four beams are large near the anchors and become thinner until they connect with the actuation area.

The minimum stress stiffening structures all have holes bordering the anchors. Designs e and h have strict compliance constraints. As a result, they have similar topology to design c but with additional cutouts near each anchor. Designs f and g have more relaxed compliance constraints. Two strategies emerge: The first consists in making a wider hole, and the second consists in making thinner connections to the membrane. Design h is very similar in topology to the design put forth by Reines *et al.* [5]. As discussed in [17], this validates the strategy used by Reines *et al.* of using cutouts to reduce stress stiffening.

In general, the minimum stress stiffening structures obtained from adding a curling constraint have holes near the actuation membrane rather than near the anchors. The compliance constraint is necessary for convergence toward a physically meaningful structure. However, its value does not seem to affect the converged topology unless it is close to $S_{\min}$. On the other hand, the curling behavior is found to correlate well with the curling constraint. When the curling constraint is relaxed, the connections to the actuation area become positioned at a 45° angle from the center of the anchors rather than aligned with it, and the connections are gradually elongated. For the structure with the most relaxed curling constraint, less material is used, and cutouts are placed near the anchors in addition to those around the actuation area. In addition, condensed versions of the variable width beams from the minimum curling design form. This demonstrates how the algorithm and formulation are capable of achieving a compromise between reducing both stress stiffening and curling.

C. Comparison of Designs in Response to Stresses

When designing a switch for low sensitivity to both in-plane biaxial stresses and out-of-plane stress gradients, a compromise must be found: flat switches often stress stiffen more, whereas switches that experience relatively little stress stiffening tend to curl more. However, as shown in Fig. 7, no direct correlation has been found between these two behaviors.

Within the set of designs considered, the fully solid, minimum compliance, and minimum curl designs stress stiffen the most and curl very little. A planar version of the design by Reines *et al.* [5], which, as discussed in Section V-A, does not include vertical anchor springs by Reines *et al.*, stress stiffens little but curls the most.

A range of behaviors is observed from the designs obtained through minimization of stress stiffening. The stiffer designs e and h stress stiffen more than the more compliant ones. Designs f, g, and h all considerably curl. This is not a surprise since no control on curling was implemented for these optimizations.

The results of the designs obtained by minimizing stress stiffening and placing a constraint on the power of deflection are well correlated with the values of P^*. The lower the value of P^*, the less curling and the more stress stiffening it experiences. This trend is particularly true for lower values of P^* since for higher values, the constraint becomes active during fewer iterations and, therefore, becomes less important to the converged solution. In addition, these designs are of higher quality than those obtained without the curling constraint: For a given amount of total deflection, they stress stiffen less. The exact reason for this has not been elucidated. However, it seems that either the volume constraint in formulation C pushes the solution toward a low-quality local minimum or the curl constraint in formulation D pushes the solution toward a high-quality local minimum or a combination of both. This is a drawback of these formulations: Since they are not convex, local minima are likely to be found. One can only strive to find high-quality minima by improving upon the formulations and algorithm.

VII. Conclusion

A capacitive RF switch configuration is systematically optimized for low stress sensitivity. The optimized switches are compared with an existing one using finite-element simulations. The power of topology optimization is demonstrated with a formulation that finds designs that compromise between stress stiffening and curling. Although the shapes of the optimized designs make intuitive sense once they have been obtained, they would be difficult to obtain with just an iterative design process, particularly if the strategies regarding cutout placement has not been preestablished. Topology optimization simplifies the process by systematically generating designs, which can and have provided insight into design strategies. In addition, control over how important it is to reduce each behavior is achieved by varying the curling constraint.

This specific formulation has been demonstrated for a capacitive RF switch. However, it is relevant for many other MEMS devices. Biaxial stresses and stress gradients are inevitable results of the MEMS fabrication process and affect the operation parameters of devices such as pressure sensors or actuated mirrors. Beyond the formulations presented here, topology optimization can be extended to other problems by creating new formulations or adopting existing ones.

References

[1] R. Mahameed and G. M. Rebeiz, "A high-power temperature-stable electrostatic RF MEMS capacitive switch based on a thermal buckle-beam actuator design," *J. Microelectromech. Syst.*, vol. 19, no. 4, pp. 816–826, Aug. 2010.

[2] D. Peroulis, S. P. Pacheco, K. Sarabandi, and L. P. Katehi, "Alleviating the adverse effects of residual stress in RF MEMS switches," in *Proc. 31st Eur. Microw. Conf.*, 2001, pp. 173–176.

[3] C. Goldsmith, D. Forehand, D. Scarbrough, I. Johnston, S. Sampath, A. Datta, Z. Peng, C. Palego, and J. C. M. Hwang, "Performance of molybdenum as a mechanical membrane for RF MEMS switches," in *Proc. IEEE Microw. Symp. Dig.*, 2009, pp. 1229–1232.

[4] L. A. Rocha, A. Cretu, and R. F. Wolffenbuttel, "Compensation of temperature effects on the pull-in voltage of microstructures," *Sens. Actuators A, Phys.*, vol. 115, no. 2/3, pp. 351–356, Sep. 2004.

[5] I. Reines, B. Pillans, and G. M. Rebeiz, "Thin-film aluminum RF MEMS switched capacitors with stress-tolerance and temperature stability," *J. Microelectromech. Syst.*, vol. 20, no. 1, pp. 193–203, Feb. 2011.

[6] H. Nieminem, V. Ermolov, S. Silanto, K. Nybergh, and T. Ryhanen, "Design of a temperature-stable RF MEM capacitor," *J. Microelectromech. Syst.*, vol. 13, no. 5, pp. 705–714, Oct. 2004.

[7] R. Mahameed and G. M. Rebeiz, "RF MEMS capacitive switches for wide temperature range applications using a standard thin-film process," *IEEE Trans. Microw. Theory Tech.*, vol. 59, no. 7, pp. 1746–1752, Jul. 2011.

[8] M. P. Bendsoe and O. Sigmund, *Topology Optimization: Theory, Methods and Applications*, 2nd ed. New York: Springer-Verlag, 2004.

[9] L. Krog, A. Tucker, M. Kemp, and R. Boyd, "Topology optimization of aircraft wing box ribs," in *Proc. Altair Technol. Conf.*, 2004, pp. 6-1–6-16.

[10] S. Verzelli and S. Di Piazza, "Structural optimization of the rear swingarm of Ducati HyperMotard," in *Proc. Altair Hyperworks Technol. Conf. Presentations*, Oct. 2007, pp. 1–19.

[11] M. A. Philippine, C.-F. Chiang, J. Salvia, C. M. Jha, S. Yoneoka, and T. Kenny, "Material distribution design for a piezoelectric energy harvester displaying geometric nonlinearity," in *Proc. Solid-State Sens., Actuators, Microsyst. Workshop*, Hilton Head, SC, 2010, pp. 451–454.

[12] O. Sigmund, "Design of multiphysics actuators using topology optimization—Part I: One-material structures," *Comput. Methods Appl. Mech.Eng.*, vol. 190, no. 49/50, pp. 6577–6604, Oct. 2001.

[13] Ö. Sardan, D. H. Petersen, K. Mlhave, O. Sigmund, and P. Bggild, "Topology optimized electrothermal polysilicon microgrippers," *Microelectron. Eng.*, vol. 85, no. 5/6, pp. 1096–1099, May/Jun. 2008.

[14] F. Okkels and H. Bruus, "Scaling behavior of optimally structured catalytic microfluidic reactors," *Phys. Rev. E., Stat., Nonlin., Soft Matter Phys.*, vol. 75, no. 1, p. 016301, Jan. 2007.

[15] K. Svanberg, "The method of moving asymptotes—A new method for structural optimization," *Int. J. Numer. Methods Eng.*, vol. 24, no. 2, pp. 359–373, Feb. 1987.

[16] F. Wang, B. S. Lazarov, and O. Sigmund, "On projection methods, convergence, and robust formulations in topology optimization," *Struct. Multidisc. Optim.*, vol. 43, no. 6, pp. 767–784, Jun. 2011.

[17] M. A. Philippine, O. Sigmund, G. M. Rebeiz, and T. W. Kenny, "Reduction of initial stress stiffening by topology optimization," in *Proc. DTIP MEMS MOEMS*, Cannes, France, 2012, pp. 148–153.

[18] E. Andreassen, A. Clausen, M. Schevenels, B. S. Lazarov, and O. Sigmund (2011, Jan.). Efficient topology optimization in MATLAB using 88 lines of code. *Struct. Multidiscpl. Optim.* [Online]. *43(1)*, pp. 1–16. Available: http://www.topopt.dtu.dk

[19] M. A. Bhatti, *Advanced Topics In Finite Element Analysis Of Structures With Mathematica and MATLAB Computations Wiley Student Companion Site*. Hoboken, NJ, 2006. [Online]. Available: http://www.wiley.com

[20] R. D. Cook, D. S. Malkus, M. E. Plesha, and R. J. Witt, *Concepts and Applications of Finite Element Analysis*, 4th ed. Hoboken, NJ: Wiley, 2001.

[21] N. L. Pedersen, "On topology optimization of plates with prestress," *Int. J. Numer. Methods Eng.*, vol. 51, no. 2, pp. 225–239, May 2001.

[22] N. L. Pedersen, "Topology optimization of laminated plates with prestress," *Comput. Struct.*, vol. 80, no. 7/8, pp. 559–570, Mar. 2002.

[23] T. Buhl, C. B. W. Pedersen, and O. Sigmund, "Stiffness design of geometrically nonlinear structures using topology optimization," *Struct. Multidiscipl. Optim.*, vol. 19, no. 2, pp. 93–104, Apr. 2000.
[24] J. K. Guest, A. Asadpoure, and S.-H. Ha, "Eliminating beta-continuation from Heaviside projection and density filter algorithms," *Struct. Multidiscipl. Optim.*, vol. 44, no. 4, pp. 443–453, Oct. 2011.
[25] G. M. Rebeiz, *RF MEMS: Theory, Design and Technology*, 1st ed. Hoboken, NJ: Wiley, 2003.

Mandy A. Philippine received the B.S. degree in mechanical engineering from the University of California, Berkeley, in 2007, and the M.S. degree in mechanical engineering from Stanford University, Stanford, CA, in 2009. She is currently working toward the Ph.D. degree in the Micro Structures and Sensors Laboratory, Stanford University.

During 2006–2007, she was an Intern at Qualcomm MEMS Technologies (QMT). Her research interests include mechanics, simulation, and topology optimization of microelectromechanical structures.

Ms. Philippine was a recipient of the National Science Foundation Graduate Research Fellowship Program.

Ole Sigmund received the M.Sc., Ph.D., and Dr. Techn. degrees in mechanical engineering from the Technical University of Denmark, Kongens Lyngby, Denmark, in 1991, 1994, and 2001, respectively.

During 1991–1992, he was a Research Assistant with the University of Essen, Essen, Germany. During 1995–1996, he was a Postgraduate Fellow with the Princeton Materials Institute, Princeton University. He is currently a Full Professor and Section Head with the Department of Mechanical Engineering, Section for Solid Mechanics, Technical University of Denmark. He has been the Principal Investigator of a number of larger nationally and internationally funded research projects. He has published more than 95 research papers in peer-reviewed international journals. He coauthored the monograph *Topology Optimization—Theory, Methods and Applications* (Springer, 2004) with M. P. Bendsøe. His principal research interests include theoretical extensions and applications of topology optimization methods to the design of extremal materials, smart materials, compliant mechanisms, microelectromechanical systems, crashworthiness, fluid systems, and wave-propagation problems in acoustics, elasticity, nanooptics, metamaterials, and antennas.

Dr. Sigmund is the Elected President of the International Society of Structural and Multidisciplinary Optimization.

Gabriel M. Rebeiz (S'86–M'88–SM'93–F'97) received the Ph.D. degree from the California Institute of Technology, Pasadena.

He is the Wireless Communications Industry Chair Professor of Electrical and Computer Engineering with the University of California, San Diego (UCSD). Prior to this appointment, he was with the University of Michigan from 1988 to 2004. From 1988 to 1996, he contributed to planar millimeter-wave and terahertz antennas and imaging arrays, and his group optimized the dielectric-lens antenna, which is the most widely used antenna at millimeter-wave and terahertz frequencies. His group also developed 6–18-GHz and 40–50-GHz 8- and 16-element phased arrays on a single silicon chip and the first millimeter-wave silicon passive imager chip at 85–105 GHz. His group also demonstrated high-Q RF MEMS tunable filters at 1–6 GHz ($Q > 200$) and the new angular-based RF MEMS capacitive and high-power high-reliability RF MEMS metal-contact switches. As a Consultant, he helped develop the *USM/ViaSat* 24-GHz single-chip SiGe automotive radar; phased arrays operating at X, Ku-band, K, Ka, Q, and W-band for defense and commercial applications; the *RFMD* RF MEMS switch; and the Agilent RF MEMS switch. He is the Director of the UCSD/DARPA Center on RF MEMS Reliability and Design Fundamentals and the author of the best seller book RF MEMS: Theory, Design and Technology (Wiley, 2003).

Dr. Rebeiz was an NSF Presidential Young Investigator, the URSI Koga Gold Medal Recipient, the 2003 IEEE MTT (Microwave Theory and Techniques) Distinguished Young Engineer, and was the recipient of the IEEE MTT 2000 Microwave Prize, the IEEE MTT 2010 Distinguished Educator Award, and the 2011 IEEE AP (Antennas and Propagation) John D. Kraus Antenna Award. He also received the 1997–1998 Eta Kappa Nu Professor of the Year Award, the 1998 College of Engineering Teaching Award, the 1998 Amoco Teaching Award given to the best undergraduate teacher at the University of Michigan, and the 2008 Teacher of the Year Award from the Jacobs School of Engineering, UCSD. His students have won a total of 20 best paper awards at the IEEE MTT, RFIC, and AP-S conferences. He has been an Associate Editor of the IEEE MTT and a Distinguished Lecturer for the IEEE MTT, IEEE AP, and IEEE Solid-State Circuits Societies. He has graduated 44 Ph.D. students and 16 postdoctoral fellows and has more than 500 IEEE publications. He currently leads a group of 21 Ph.D. students and postdoctoral fellows in the area of millimeter-wave RFIC, tunable microwave circuits, RF MEMS, planar millimeter-wave antennas, and terahertz systems.

Thomas W. Kenny received the B.S. degree in physics from the University of Minnesota, Minneapolis, in 1983, and the M.S. and Ph.D. degrees in physics from the University of California, Berkeley, in 1987 and 1989, respectively.

From 1989 to 1993, he was with the Jet Propulsion Laboratory, National Aeronautics and Space Administration, Pasadena, CA, where his research focused on the development of electron-tunneling high-resolution microsensors. In 1994, he joined the Department of Mechanical Engineering, Stanford University, Stanford, CA, where he directs microsensor-based research in a variety of areas, including resonators, wafer-scale packaging, cantilever beam force sensors, microfluidics, and novel fabrication techniques for micromechanical structures. He is the Founder and CTO of Cooligy, Sunnyvale, CA, a microfluidics chip cooling component manufacturer, and the Founder and a Board Member of SiTime Corporation, a developer of CMOS timing references using MEMS resonators. He is currently a Stanford Bosch Faculty Development Scholar and was the General Chairman of the 2006 Hilton Head Solid State Sensor, Actuator, and Microsystems Workshop. From October 2006 to September 2010, he was on leave to serve as Program Manager with the Microsystems Technology Office, Defense Advanced Research Projects Agency, where he started and managed programs in thermal management, nanomanufacturing, manipulation of Casimir forces, and the Young Faculty Award. He has authored or coauthored over 250 scientific papers and is the holder of 48 issued patents.